Development and Validation of the Rensselaer Multicopter Analysis Code (RMAC): A Physics-Based Comprehensive Modeling Tool

Robert Niemiec
Research Scientist

Farhan Gandhi
Redfern Chair of Aerospace Engineering

Center for Mobility with Vertical Lift (MOVE)
Rensselaer Polytechnic Institute
Troy, NY, United States

ABSTRACT

A comprehensive analysis tool (RMAC) is developed and validated for use on small-scale multi-rotor aircraft. RMAC can model multicopters with arbitrary rotor number, orientation, and position as a 6-DOF rigid-body dynamic system. Several induced-flow models, from momentum-theory to vortex-wake are available for rotor aerodynamic analysis, and rotor dynamics can optionally be modeled using the Hodges-Dowell equations. RMAC is capable of determining trim conditions, as well as generate linear models and provide nonlinear simulation in Simulink. Isolated rotor loads are validated against experimental data, with hover loads predicted as well as the analysis tool CAMRAD II. In forward flight, trends are captured well by RMAC. Predictions of the linear dynamics of the University of Portland Hexacopter are compared against experimental data, with adequate accuracy for the development of linear feedback controllers.

NOTATION

Acronyms

CG	Center of Gravity
DOF	Degree of Freedom
eVTOL	Electric Vertical Takeoff and Landing
RMAC	Rensselaer Multicopter Analysis Code
RHS	Right-Hand-Side

Symbols

$c_\square$	Cosine Function
C_T	Thrust Coefficient
$\vec{D}_f$	Fuselage Drag
EA	Blade Axial Stiffness
EI	Blade Flexural Stiffness
$\vec{F}_j$	Force Vector of rotor j, acting at its hub
I	Aircraft Inertia Tensor
k_x, k_y	Longitudinal and Lateral Inflow Slope
$L^\square$	Wake Influence Coefficient Matrix
$M^\square$	Peters-He Mass Matrix
$\vec{M}_j$	Moment vector of rotor j, about its own hub
p, q, r	Aircraft Angular Velocity Components (Body Frame)
$\vec{r}$	Displacement Vector from aircraft CG
${}^BR^A$	Rotation Matrix from Frame A to Frame B
$s_\square$	Sine Function
$t_\square$	Tangent Function
T	Axial tension in rotor blade
u, v, w	Aircraft Velocity Components (Body Frame)
U, V, W	Axial, In-plane, and out-of-plane elastic blade deformation
$\vec{V}$	Linear Velocity Vector
x, y, z	Aircraft Position
X	Aircraft State vector
α	Peters-He Inflow State
θ_b	Local Blade Pitch
λ	Inflow Ratio
μ	Advance Ratio $V/\Omega R$
ρ	Ambient Density
τ	Peters-He Forcing Function
ϕ_n^m	Peters-He Inflow Polynomial Shape Function
ϕ, θ, ψ	Aircraft Roll, Pitch, Yaw Attitude
χ	Wake Skew Angle
$\vec{\omega}$	Angular Velocity Vector

Left Superscripts

B	Body Reference Frame
H	Hub-Wind Reference Frame
I	Inertial Reference Frame

Right Superscripts

m	Peters-He Harmonic Number
s, c	Sine/Cosine

Right Subscripts

n	Peters-He Polynomial Number
x, y, z	Direction of vector component
HD	Hodges-Dowell
PH	Peters-He
RB	Rigid Body

Presented at the Vertical Flight Society 75th Annual Forum & Technology Display, Philadelphia, Pennsylvania, May 13–16, 2019.

INTRODUCTION

Electric Vertical Takeoff and Landing (eVTOL) aircraft have generated an enormous amount of interest in recent years, with low barriers to entry enabling start-ups (Refs. 1–4) and large companies, both new to VTOL (Refs. 5, 6) and those already established in the field (Refs. 7, 8) to produce designs and prototypes. Much of this interest is associated with Uber Elevate (Ref. 9), which seeks to provide an air-taxi service between cities and their suburbs. The NASA Urban Air Mobility Grand Challenge (Ref. 10), which seeks to integrate vehicles and airspace management to enable large-scale eVTOL operations within cities, is also a driving factor in eVTOL research.

Within the community of controls engineering, a lot of work has been done on multicopters. For their work, these researchers have relied on simple models to predict the forces and moments produced by the rotors. For the most part, these studies rely on the Ω^2 model (Eq. 1) (Refs. 11, 12), where the thrust and (magnitude of) the torque produced by the rotor are proportional to the square of the rotor rotational speed. The proportionality constants are usually obtained experimentally via static thrust tests (Ref. 13). This model, while accurate for hover, ignores the drag, side force, and pitching and rolling moments that are produced in forward flight.

$$\begin{aligned} \text{Thrust} &= a\Omega^2 \\ \text{Torque} = b\Omega^2 &\Rightarrow \text{Power} = b\Omega^3 \end{aligned} \tag{1}$$

As eVTOL aircraft become more widespread, physics-based analyses are increasingly necessary to predict performance and design control laws, and to design an aircraft that can safely execute a mission. At the high-end of fidelity is Computational Fluid Dynamics (CFD), which numerically solve conservation equations (usually Navier-Stokes) in a fluid domain around a rotor. CFD has been applied to eVTOL to identify complex aerodynamic interactions, such as those between the rotors and the fuselage (Ref. 14), and between the rotors themselves (Ref. 15). These analyses, though they are very accurate and can capture extremely complex flow features, require many hours on hundreds or even thousands of CPU cores to produce a prediction at a single condition.

Lower fidelity models use simplified physics to capture most of the physical phenomena at little computational expense. For helicopters, models are usually based on blade element theory (Ref. 16), which calculates aerodynamic forces on 2-dimensional sections along the blade, and integrates to find the total load. These techniques are extensively used in conventional VTOL design; some common tools are the Rotorcraft Comprehensive Analysis System (RCAS) (Ref. 17), Comprehensive Analysis Modeling for Rotorcraft Aerodynamics and Dynamics II (CAMRAD II) (Ref. 18), and the University of Maryland Advanced Rotorcraft Code (UMARC) (Ref. 19). These codes are well-established for, but are tailored to, conventional helicopters, which have some key differences to multicopters. In particular, these codes often assume a fixed RPM for their rotors, as well as the presence of cyclic pitch controls and flapping hinges or flexures. Multicopters generally operate on the assumption that the rotors are fixed-pitch, and use their speed to regulate the forces and moments on the aircraft.

This paper presents a new comprehensive analysis model, specifically designed to analyze multicopters, the Rensselaer Multicopter Analysis Code (RMAC). Like other models, it uses simple physics to generate predictions of the performance and dynamic behavior of multicopters. RMAC is capable of conducting trim analysis, generating linear models for control design, and fully nonlinear simulation in Simulink. This paper will begin with an overview of the modeling options available within RMAC, and will be followed by validation of the code for isolated rotor loads in hover and forward flight, and finally a validation of the linearized dynamics against flight data.

AIRCRAFT DEFINITION

An aircraft model can be defined in two ways in RMAC: directly through an ASCII file, or through a Graphical User Interface (Fig. 1). Within this GUI, several geometric parameters of the aircraft can be defined, and a preview of the aircraft is illustrated. The GUI currently only allows the creation of a regular multicopter, which is defined as a multicopter with an even number of identical rotors (except for spin direction) arranged in a regular n-gon, though through the ASCII file, an arbitrary multicopter can be defined. The number of rotors, their radius, length of the booms to which they are attached, and the rotor hubs' vertical displacement from the aircraft center of gravity are all defined in this GUI. Additionally, whether the aircraft operates edge-first (with two rotors leading the aircraft) or vertex-first (with one) and whether rotor 1 (the front-most starboard rotor for edge-first, front rotor for vertex-first configurations) spins clockwise (colored red) or counterclockwise (colored blue). Finally, the orientation of the rotors (using multi-rotor coordinates as in (Ref. 20)) can be defined in a pop-up window.

The rotor geometry GUI (Fig. 2) can be accessed by clicking the "Rotors" tab on the Aircraft Geometry GUI. Here, the rotor geometry can be defined in detail, and a top-down preview of the rotor is provided. The number of blades, effective root cut-out (inboard of which no aerodynamic loads are modeled), and the radius can be defined on this window. Additionally, the chord can be defined as an arbitrary piecewise linear distribution. Local values of chord can be defined either in absolute terms, or in terms of solidity. If the latter is chosen, the chord is scaled as the number of blades or rotor radius change. Similarly, the twist and airfoil distributions are defined as piecewise linear.

Rotors and aircraft can be saved or loaded as ASCII files by clicking the "Save" or "Load" buttons on their respective windows. Aerodynamic model parameters (currently restricted to the induced flow model only) are defined in the "Model" tab visible in Figs. 1 and 2. Upon closing the window, the user is prompted to save the aircraft and model parameters into a case

file, which allows RMAC to load the ASCII files generated by the GUI.

AIRCRAFT DYNAMICS MODEL

An arbitrary multicopter is modeled as a 6DOF, second-order dynamic system. Linear and angular accelerations are calculated by summing forces and moments acting on the aircraft. The six states of this model are a three-dimensional position, and three Euler angles, describing a 3-2-1 rotation from a fixed, North-East-Down reference frame (referred to as the inertial frame), and a body-attached reference frame, illustrated in Fig. 3. The direction cosines matrix used to express vectors defined in the inertial frame in the body frame is given by Eq. 2. The inverse of this rotation matrix is its transpose, which is used to express vectors defined in the body frame in the inertial frame.

$$ {}^{I}R^{B} = \begin{bmatrix} c_\theta c_\psi & c_\theta s_\psi & -s_\theta \\ s_\phi s_\theta c_\psi - c_\phi s_\psi & s_\phi s_\theta s_\psi + c_\phi c_\psi & s_\phi c_\theta \\ c_\phi s_\theta c_\psi + s_\phi s_\psi & c_\phi s_\theta s_\psi - s_\phi c_\psi & c_\phi c_\theta \end{bmatrix} \tag{2} $$

$$ {}^{B}R^{I} = ({}^{I}R^{B})^{T} $$

RMAC allows rotors to be oriented arbitrarily relative to the fuselage. To simplify rotor aerodynamic analysis, an additional reference frame is defined at the hub of each rotor, as illustrated in Fig. 4. In the hub reference frame, the negative z-axis is aligned with the rotor thrust, and the positive x-axis is oriented such that the relative wind contains no y-component.

By introducing six kinematic equations, the 6-state, second-order rigid body dynamics can be expressed as an identical 12-state, first-order dynamic system. The rigid-body state vector is given by Eq. 3. The position of the aircraft in the inertial reference frame is defined by the states (x, y, z), and the attitude is defined by the states (ϕ, θ, ψ). The states (u, v, w) are the x-, y-, and z-components of the velocity in the body reference frame, and finally (p, q, r) are the angular velocity components in the body-attached reference frame. The kinematic equations of motion are given by Eqs. 4 and 5, which define the evolution of the position and orientation of the aircraft, respectively. Due to the choice of Euler angles, there is a singularity in Eq. 5 at $\theta = \pm 90^\circ$. This singularity prevents RMAC from simulating extremely aggressive pitch maneuvers.

$$ X_{RB} = \begin{bmatrix} x & y & z & \phi & \theta & \psi & u & v & w & p & q & r \end{bmatrix}^{T} \tag{3} $$

$$ \begin{bmatrix} \dot{x} \\ \dot{y} \\ \dot{z} \end{bmatrix} = {}^{I}R^{B} \begin{bmatrix} u \\ v \\ w \end{bmatrix} = {}^{I}R^{B} \cdot {}^{B}\vec{V} \tag{4} $$

$$ \begin{bmatrix} \dot{\phi} \\ \dot{\theta} \\ \dot{\psi} \end{bmatrix} = \begin{bmatrix} 1 & s_\phi t_\theta & c_\phi t_\theta \\ 0 & c_\phi & -s_\phi \\ 0 & s_\phi / c_\theta & c_\phi / c_\theta \end{bmatrix} \begin{bmatrix} p \\ q \\ r \end{bmatrix} \tag{5} $$

The derivatives of the linear velocity states are given by Eq. 6. The first two terms on the RHS in Eq. 6 represent gravity and fuselage forces (treated as a point force at the center of pressure of the aircraft, displaced from the C.G. by ${}^{B}\vec{r}_D$), respectively. The summation on the RHS represents the forces, including thrust, drag, and side force, produced by each rotor on the aircraft. The final term represents the Coriolis force, as the body-frame is non-inertial.

$$ m \begin{bmatrix} \dot{u} \\ \dot{v} \\ \dot{w} \end{bmatrix} = mg({}^{B}R^{I} \cdot {}^{I}\hat{z}) + {}^{B}\vec{D}_f + \sum_{j=1}^{n_{rotors}} {}^{B}\vec{F}_j - m\left({}^{B}\vec{\omega} \times {}^{B}\vec{V} \right) \tag{6} $$

The angular dynamics are given by Eq. 7. On the RHS, the first term is the moment produced by aerodynamic forces on the fuselage, the final term is the gyroscopic moment, and the summation term accounts for both the aerodynamic moments evaluated at the hub of each rotor ($\vec{M}_j$) and the force-induced moments about the C.G.

$$ {}^{BB}I \begin{bmatrix} \dot{p} \\ \dot{q} \\ \dot{r} \end{bmatrix} = {}^{B}\vec{r}_D \times {}^{B}\vec{D}_f + \sum_{j=1}^{n_{rotors}} \left({}^{B}\vec{M}_j + {}^{B}\vec{r}_j \times {}^{B}\vec{F}_j \right) - {}^{B}\vec{\omega} \times {}^{BB}I \cdot {}^{B}\vec{\omega} \tag{7} $$

Rotor Model

Blade Element Theory ((Refs. 16, 21) is used to determine the aerodynamic loading on each rotor. Essential to the accurate calculation of lift and drag is an appropriate induced-flow model. RMAC includes several options for induced-flow models, including finite-state dynamic wake and vortex-wake models, the implementation of which are detailed in this section. Simpler, less expensive, momentum-theory based models are also available in RMAC.

Momentum Theory-Based Inflow The simplest inflow model available in RMAC is a uniform inflow model, with the mean value of the inflow following Eq. 8, where μ_z and mu_x are, respectively, the components of the freestream velocity normal to (positive for descent) and in the plane of the rotor, normalized by the hover tip speed. The Drees linear inflow model, represented by Eq. 9 is also implemented in RMAC, but is not recommended for fixed-pitch multicopters (Ref. 22). Tip losses are modeled using the Prandtl tip loss function, scaling the lift produced by Eq. 10.

$$ \lambda = -\mu_z + \lambda_0 = -\mu_z + \frac{C_T}{2\sqrt{\mu_x^2 + \lambda^2}} \tag{8} $$

$$ \lambda(\bar{r}, \psi) = \lambda_0 (1 + k_x \bar{r} \cos\psi + k_y \bar{r} \sin\psi) $$
$$ k_x = \frac{4}{3}\left(\frac{1 - \cos\chi - 1.8\mu^2}{\sin\chi} \right) \qquad k_y = -2\mu \tag{9} $$
$$ \chi = \text{atan2}(\mu_x, -\mu_z + \lambda_0) $$

$$F = \left(\frac{2}{\pi}\right)\cos^{-1}\left(e^{-f}\right)$$
$$f = \frac{N_b}{2}\left(\frac{1-r}{\lambda}\right) \tag{10}$$

Finite State Dynamic Wake The finite state dynamic wake model implemented in RMAC is the generalized Peters-He model (Ref. 23). Fundamentally, this model is a Galerkin method applied to the linearized Euler equations, with an assumed skewed cylindrical wake structure. The number of modes taken is determined by two parameters m_max, which represents the maximum harmonic number in the shape functions, and n_max, which determines the highest-order polynomial in the radial direction. The induced flow distribution (normalized by rotor tip speed ΩR) as a function of the radial and azimuthal locations on the rotor are given by Eq. 11, where α_n^{mc} and α_n^{ms} are the dynamic states of the rotor wake, and are unique to each rotor. For $m = 0$, α_n^{ms} has no effect on the induced flow ($\sin 0 = 0$), and is excluded from the model.

$$\lambda(\bar{r},\psi) = \sum_{m=0}^{m_{max}} \sum_{n=m+1,m+3,\cdots}^{n_{max}} \phi_n^m(\bar{r})\left(\alpha_n^{mc}\cos m\psi + \alpha_n^{ms}\sin m\psi\right) \tag{11}$$

The dynamic equations take the form of Eq. 12, where the $\star$ operator represents a derivative with respect to time, normalized by the rotor speed Ω. The matrices M and L are available in closed form in (Ref. 23). τ represents the aerodynamic forcing, and is calculated from the rotor circulatory lift by Eq. 13. Eq. 12 is repeated for each rotor, which generally have unique inflow states. The state vector for the inflow is given in Eq. 14

$$\begin{bmatrix} M^c & 0 \\ 0 & M^s \end{bmatrix} \begin{Bmatrix} \overset{\star}{\alpha}^c \\ \overset{\star}{\alpha}^s \end{Bmatrix} + [V] \begin{bmatrix} L^c & 0 \\ 0 & L^s \end{bmatrix}^{-1} \begin{Bmatrix} \alpha^c \\ \alpha^s \end{Bmatrix} = \begin{Bmatrix} \tau^c \\ \tau_s \end{Bmatrix} \tag{12}$$

$$\tau_n^{mc} = \begin{cases} \frac{1}{2\pi}\sum_{q=1}^{n_{blades}} \int_0^1 \frac{L_q}{\rho\Omega^2R^3}\phi_n^0(\bar{r})d\bar{r} & m = 0 \\ \frac{1}{\pi}\sum_{q=1}^{n_{blades}} \int_0^1 \frac{L_q}{\rho\Omega^2R^3}\phi_n^m(\bar{r})d\bar{r}\cos(m\psi_q) & m > 0 \end{cases}$$
$$\tau_n^{ms} = \frac{1}{\pi}\sum_{q=1}^{n_{blades}} \int_0^1 \frac{L_q}{\rho\Omega^2R^3}\phi_n^m(\bar{r})d\bar{r}\sin(m\psi_q) \tag{13}$$

$$X_{PH} = \begin{bmatrix} \alpha_1^{cT} & \alpha_1^{sT} & \alpha_2^{cT} & \alpha_2^{sT} & \cdots & \alpha_N^{cT} & \alpha_N^{sT} \end{bmatrix}^T \tag{14}$$

When performing trim analysis, τ is averaged over a rotor revolution, and Eq. 12 is solved such that $\overset{\star}{\alpha} = 0$. Mathematically speaking, this is identical to performing a harmonic balance with only a steady component. Tip losses are again modeled using Eq. 10. Because the aerodynamic forcing is a function only of the rotor's own lift, each rotor's inflow dynamics are decoupled when this model is used. This simplifies the dynamics, but neglects rotor-rotor interference effects, which are known to be significant in forward flight (Refs. 15, 24).

Vortex Wake Both a prescribed wake and free wake model are implemented in RMAC. Since the Biot-Savart Law allows the computation of induced velocities anywhere in space, they can be used to model rotor-rotor interference, at the expense of relatively large computational effort, particularly for free-wake models. For the prescribed wake model, a rigid, helical wake geometry is assumed, while for the free-wake, the instantaneous geometry of the wake is used to calculate local velocities, which is used to evolve the geometry over time. In both of these models, the strength of the vortices is a function of the circulation bound in the rotor blades, which is calculated using lifting-line theory. Tip losses are directly modeled when vortex wake methods are used, so no additional tip loss model is necessary.

To solve the equations introduced by prescribed wake (vortex strength) and free wake (vortex strength and geometry), two basic approaches are used: time-accurate (Ref. 25) relaxation methods (Ref. 26). In the former, the equations of motion for the rotor wake geometry are directly integrated, which allows the model to capture not only steady-state operation, but maneuvers or other unsteady phenomena. The latter approach assumes periodicity (with a period equal to one rotor revolution) in the rotor wake, which allows a fixed-point iteration scheme to capture the geometry of the rotor (at lower computational cost than time-accurate methods), but restricts the model to steady-state operation. Because the rotors of a multicopter generally operate at different rotational speeds, the interference effects between rotors will vary from revolution to revolution as the relative phase of the rotors changes. Though the conditions are still technically periodic, it is possible to implement relaxation methods in steady operation, but the period is prohibitively long. Thus, time accurate methods are used for free-wake in RMAC.

Blade Dynamics Model The nonlinear elastic blade model of Hodges and Dowell (Ref. 27) is implemented in RMAC, and the equations of motion, neglecting elastic torsion, are given in Eqs. 15-17. The Hodges-Dowell equations are simplified by the assumption that the elastic axis, tensile axis, and locus of mass centroids are coincident. The constitutive equation relating the tension in the blade and the deformation is given by Eq. 18. Because the dynamics in axial extension are higher-order Eqs. 15 and 18 can be used to solve for carried tension, T, and axial displacement, U, in terms of in-plane displacement, V, and out-of-plane displacement, W.

$$-T' - m(\Omega^2 r + 2\Omega\dot{V}) = 0 \tag{15}$$

$$-(TV')' + \left\{\left(EI_z\cos^2\theta_b + EI_y\sin^2\theta_b\right)V'' + \left(EI_z - EI_y\right)\cos\theta_b\sin\theta_b W''\right\}'' + 2m\Omega\dot{u} + m\ddot{V} - m\Omega^2 V = L_V \tag{16}$$

$$-(TW')' + \left\{ \left(EI_z + EI_y\right)\cos\theta_b \sin\theta_b V'' + \left(EI_z \sin^2\theta_b + EI_y \cos^2\theta_b\right) W'' \right\}'' + m\ddot{W} = L_W \quad (17)$$

$$T = EA\left\{ U' + \frac{V'^2 + W'^2}{2} \right\} \quad (18)$$

The partial differential equations are discretized in space using the Galerkin method, where

$$\begin{aligned} W(\bar{r},t) &= \sum_{i=1}^{n_W} \phi_i(\bar{r}) q_{W,i}(t) \\ V(\bar{r},t) &= \sum_{i=1}^{n_V} \phi_i(\bar{r}) q_{V,i}(t) \end{aligned} \quad (19)$$

The functions ϕ_i are chosen to satisfy the clamped-free boundary conditions, and to be orthogonal to one another with respect to the L_2 inner product, or, expressed mathematically,

$$\begin{aligned} \phi_i(0) &= 0 & \phi_i''(1) &= 0 \\ \phi_i'(0) &= 0 & \phi_i'''(1) &= 0 \\ & \phi_i(1) = 1 & & \\ \int_0^1 \phi_i(\bar{r})\phi_j(\bar{r}) d\bar{r} &= 0 & i &\neq j \end{aligned} \quad (20)$$

Substituting Eq. 19 into Eqs. 16 and 17, and manipulating into the Galerkin form results in a system of second-order ordinary differential equations of the form Eq. 21, where all of the nonlinear terms are included in the forcing. Eq. 21 is solved for each rotor in equilibrium using a harmonic balance, assuming that the deflections are periodic over one rotor revolution. In dynamic simulation, the second-order ODEs are recast into first-order ODEs by introducing kinematic variables (Eq. 22).

$$\begin{bmatrix} M_{vv} & M_{vw} \\ M_{wv} & M_{ww} \end{bmatrix} \begin{Bmatrix} \ddot{q}_V \\ \ddot{q}_W \end{Bmatrix} + \begin{bmatrix} K_{vv} & K_{vw} \\ K_{wv} & K_{ww} \end{bmatrix} \begin{Bmatrix} q_V \\ q_W \end{Bmatrix} = \begin{Bmatrix} F_V \\ F_Q \end{Bmatrix} \quad (21)$$

$$\begin{aligned} \begin{Bmatrix} \dot{q}_V \\ \dot{q}_W \end{Bmatrix} &= \begin{Bmatrix} v_V \\ v_W \end{Bmatrix} \\ \begin{Bmatrix} \dot{v}_V \\ \dot{v}_W \end{Bmatrix} &= [M]^{-1} \left[\begin{Bmatrix} F_V \\ F_Q \end{Bmatrix} - [K] \begin{Bmatrix} q_V \\ q_W \end{Bmatrix} \right] \end{aligned} \quad (22)$$

The dynamic states associated with the Hodges-Dowell elastic deformation are expressed in individual blade coordinates (Ref. 28), and for N-bladed rotors are given by Eq. 23.

$$X_{HD} = \begin{bmatrix} q_{V,1}^T & q_{W,1}^T & v_{V,1}^T & v_{W,1}^T & \cdots & v_{W,N}^T \end{bmatrix}^T \quad (23)$$

Rotor Rotational Dynamics In order to convert between multi-blade and individual blade coordinates, the azimuthal position of each rotor blade must be tracked, and kinematic equations must be introduced (Eq. 24). Because the rotor speeds can change dramatically throughout flight, Eq. 24 must be integrated numerically along with the kinematic and dynamic states of the aircraft.

$$\dot{\psi}_k = \Omega_k(t) \quad (24)$$

If desired by the user, RMAC can model the rotational dynamics of the rotor by conservation of angular momentum, Eq. 25, where I_k is the inertia of rotor k, and Q_k is the torque applied by its motor. If rotational dynamics are included, the torque is used as a control input, while if they are neglected, the rotor speed Ω is used directly to control the aircraft.

$$\dot{\Omega}_k = \frac{1}{I_k}(Q_n - Q_{aero,k}) \quad (25)$$

Dynamic Equations of Motion

The dynamic equations of motion for the multicopter take the form of Eq. 26, where f and g are vector-valued dynamic equations and output equations, respectively. f is a concatenation of Eqs. 6, 7, 12, 22, 24, and 25, or a subset of these, as desired by the user.

$$\begin{aligned} \dot{X} &= f(X,u) \\ y &= g(X,u) \end{aligned} \quad (26)$$

TRIM ALGORITHM

To determine equilibrium, the output function g is defined to output the linear and angular accelerations, and any other algebraic equation that must be satisfied. As examples, the difference between assumed Fourier coefficients in the elastic blade model (used to calculate aerodynamic loads) and actual response (from Eq. 21), or consistency between the thrust coefficient used to solve Eq. 8 and the thrust produced by the rotor. To solve the six rigid-body equilibrium equations, four primary control inputs (Ref. 29) and the roll and pitch attitudes are used can be used as output equations.

A Newton-Raphson method is used to determine equilibrium conditions. First, a value for x_e and u_e is assumed, and the output function is evaluated. Next, x_e and u_e are updated by Eq. 27, where J_x and J_u are given by Eq. 28. The operator denoted by the superscript $+$ is the Moore-Penrose pseudoinverse for underdetermined systems, Eq. 29. For an invertible matrix, $J^+ = J^{-1}$. The matrices J_x and J_u are determined numerically by forward difference.

$$\begin{Bmatrix} X_e^{(n+1)} \\ u_e^{(n+1)} \end{Bmatrix} = \begin{Bmatrix} X_e^{(n)} \\ u_e^{(n)} \end{Bmatrix} - \begin{bmatrix} J_X & J_u \end{bmatrix}^+ g(X_e^{(n)}, u^{(n)}) \quad (27)$$

$$J_{X,ij} = \frac{\partial g_i}{\partial X_j} \qquad J_{u,ij} = \frac{\partial g_i}{\partial u_j} \tag{28}$$

$$J^+ = J^T (JJ^T)^{-1} \tag{29}$$

Iteration of the Newton-Raphson loop is terminated when either of two criteria is met. The first is an absolute tolerance on the 1-norm of g. The other is a relative (to the input size) tolerance on the update step. If the error is sufficiently small (default value of 10^{-6}) or the update step is small (default value 10^{-2}), the trim loop terminates successfully. To avoid infinite loops, the solution procedure will terminate if a maximum number of iterations (default 50) are performed, with a flag indicating that the solution was unsuccessful. To improve the stability of the algorithm, a relaxation parameter (default 0.5) is used to reduce the update step.

LINEAR FLIGHT DYNAMICS MODELING

Upon determining an equilibrium point, the dynamics can be linearized numerically into the form of Eq. 30, where A, B, C, and D are given by Eq. 31, and x and u now represent deviations from the equilibrium point (x_e, u_e). All matrices are estimated by applying a two-point centered difference stencil to f and g. The eigenvectors of A represent the dynamic modes of the bare airframe, and their associated eigenvalues indicate their stability and damping.

$$\begin{aligned} \dot{X} &= AX + Bu \\ y &= CX + Du \end{aligned} \tag{30}$$

$$\begin{aligned} A_{ij} &= \frac{\partial f_i}{\partial X_j} & B_{ij} &= \frac{\partial f_i}{u_j} \\ C_{ij} &= \frac{\partial g_i}{\partial X_j} & D_{ij} &= \frac{\partial g_i}{\partial u_j} \end{aligned} \tag{31}$$

To simplify the linear dynamics, states that are well-damped and high frequency can be removed from the model through static condensation. For this, x is partitioned into two components, one corresponding to "fast" dynamics (such as the inflow dynamics), and one corresponding to "slow" dynamics (such as the rigid body dynamics). Eq. 30 becomes Eq. 32. To apply static condensation, assume $\dot{X}_f = 0$. This assumption allows the second row of Eq. 32a to be solved for X_f (Eq. 33). Substitution into the first half of Eq. 32a and Eq. 32b yields the reduced system 34.

$$\begin{Bmatrix} \dot{X}_s \\ \dot{X}_f \end{Bmatrix} = \begin{bmatrix} A_{ss} & A_{sf} \\ A_{fs} & A_{ff} \end{bmatrix} \begin{Bmatrix} X_s \\ X_f \end{Bmatrix} + \begin{bmatrix} B_s \\ B_f \end{bmatrix} u \tag{32a}$$

$$y = \begin{bmatrix} C_s & C_f \end{bmatrix} \begin{Bmatrix} X_s \\ X_f \end{Bmatrix} + Du \tag{32b}$$

$$X_f = -A_{ff}^{-1}(A_{fs}X_s + B_f u) \tag{33}$$

$$\begin{aligned} \dot{X}_s &= (A_{ss} - A_{sf}A_{ff}^{-1}A_{fs})X_s + (B_s - A_{sf}A_{ff}^{-1}B_f)u \\ y &= (C_s - C_f A_{ff}^{-1}A_{fs})X_s + (D - C_f A_{ff}^{-1}B_f)u \end{aligned} \tag{34}$$

VALIDATION

Isolated Rotor

RMAC-generated predictions of the steady-state loads of isolated rotors have been compared to other, similarly complex codes, such as CAMRAD II (Ref. 18), and the higher-order computational fluid dynamics code AcuSolve (Ref. 30), as well as experimental data.

SUI Endurance The Straight-Up Imaging (SUI) Endurance (Ref. 31) is a 3.2kg quadcopter driven by four, 15-inch propellers. The chord and pitch distribution of this propeller were obtained from are given in Fig. 5. Figures 6 and 7 respectively show the thrust predicted with several modeling tools versus the rotor speed in RPM. Both the CAMRAD II and experimental data are sourced from Russel et. al (Ref. 32), from which the SUI rotor geometry and 2D aerodynamic tables are sourced. Also included in Figs. 6 and 7 are results from the finite-element CFD code AcuSolve (Ref. 15), and from the finite-volume CFD code OVERFLOW (Ref. 14). RMAC predicts the thrust as reliably (within 4%) as CAMRAD II with vortex-wake methods predicting the rotor-induced flow, though both codes overpredict the thrust (RMAC by 13.7%, and CAMRAD by 9.1-16.4% at 4500 RPM), relative to high-order CFD and experiment. The predicted aerodynamic torque in hover is plotted against rotor speed in Fig. 7. As with thrust, RMAC overpredicts the torque (by 32.0% at 4500 RPM), relative to experiment, similar to CAMRAD (which overpredicts torque by 37.7% at 4500 RPM). CAMRAD and RMAC predict the same torque within 5% at most speeds. AcuSolve offers a better prediction of rotor torque, and OVERFLOW produces results similar to RMAC.

Russell et. al also performed wind tunnel experiments on the SUI Endurance rotor, and the conditions are available (Ref. 32). The wind tunnel speed was set to 6.1 m/s (20 ft/s) and the rotor speed was varied from 2000 RPM to 4500 RPM. This test was repeated for rotor orientations between 0° and 20° nose-down. These conditions were replicated in RMAC, and the results are shown in Figs. 8-10. As in hover, thrust (Figs. 8c-10c) and torque (Figs. 8f-10f) are overpredicted, though differences become smaller as the nose-down attitude increases. Drag (Figs. 8a-10a) predictions are very similar to the experimental data, and well within the (admittedly large) error bars in the experimental data, especially at low rotor speeds. Side force (Figs. 8b-10b) is consistently underpredicted in all conditions. Rolling moment (Figs. 8d-10d) are also reasonably well-predicted.

AeroQuad Cyclone The AeroQuad Cyclone was a commercially available almost-ready-to-fly quadcopter kit. It has a gross weight of 2kg, and is driven by four, 12-inch diameter rotors. This rotor was modeled in AcuSolve (Ref. 15) at several rotational speeds, and the geometry is given in Fig. 11. The conditions of the simulation are summarized in Table 1. The overall forces and moments for these rotors are tabulated

in Table 2. Thrust and torque are predicted within 1.3% and 4.3% of the CFD predictions, respectively, while pitch and roll are underpredicted by larger margins. The thrust and torque distribution on the rotor disk are plotted in Figs. 12 and 13, respectively. As expected, the lift on the advancing (right in Fig. 12) side of the rotor disk is greater than that on the retreating (left) side of the rotor disk, due to the absence of longitudinal cyclic pitch. Additionally, greater lift is predicted by both RMAC and AcuSolve on the front (top) of the rotor than on the rear (bottom), due to the longitudinal inflow distribution in forward flight (Ref. 22). The torque coefficient distributions predicted by RMAC and AcuSolve are also qualitatively similar.

Table 1: AeroQuad Cyclone simulation conditions

Parameter	Value (Unit)
Rotor Speed	4495 (RPM)
Wind Speed	10 (m/s)
Rotor Angle of Attack	5 (degrees, nose-down)

Table 2: AeroQuad Cyclone rotor loads at 4495 RPM, 10 m/s, and 5° nose-down attitude

Load (Units)	AcuSolve	RMAC	%Error
Thrust (N)	6.25	6.33	+1.3%
Torque (Nm)	0.0930	0.0890	-4.3%
Pitch Moment (Nm)	0.115	0.105	-8.7%
Roll Moment (Nm)	0.128	0.106	-16.9%

Aircraft Dynamics

University of Portland Hexacopter The University of Portland (UP) Hexacopter (Fig. 14) is a 3.4lb hexacopter with 10-inch diameter rotors. System identification was performed on this hexacopter using CIFER (Ref. 33), and the dynamic models in hover and forward flight are compared in (Ref. 34).

In order to compare the models produced by RMAC to those identified using CIFER, the inputs and outputs must be on the same scale. The inputs used in the CIFER-identified model are pilot stick inputs, normalized on a scale of [0,1] for collective, and [-1,1] for the roll, pitch, and yaw commands. RMAC, on the other hand, commands rotor speeds directly (using multi-rotor coordinates) in radians per second. A control mixer (Eq. 35) was identified and applied to convert the inputs of the RMAC models to match those of the identified models. The rotors are modeled using a 3x4 Peters-He dynamic inflow, and are assumed to be rigid. Rotor dynamics and sensor delay are also not directly included in the RMAC results, so a lag filter and a time delay were added to RMAC results to represent their respective effects.

$$\begin{Bmatrix} \Omega_0 \\ \Omega_{1s} \\ \Omega_{1c} \\ \Omega_d \end{Bmatrix} = \begin{bmatrix} 1047 & 0 & 0 & 0 \\ 0 & -406 & 0 & 0 \\ 0 & 0 & -381 & 0 \\ 0 & 0 & 0 & 340 \end{bmatrix} \begin{Bmatrix} \delta_{\text{col}} \\ \delta_{\text{lat}} \\ \delta_{\text{lon}} \\ \delta_{\text{ped}} \end{Bmatrix} \tag{35}$$

Hover Dynamics In hover, the symmetric nature of the hexacopter decouples the dynamics. The heave dynamics are first-order, and are represented by Eq. 36, where Z_w represents heave damping, and $M_{\delta_{\text{col}}}$ represents the sensitivity of heave to collective stick input. The values identified by CIFER and estimated by RMAC are presented in Table 3. A Bode plot of the transfer function from collective stick input to heave rate is given in Fig. 15, which shows that both the magnitude and phase of the response are well-predicted by RMAC, though the overprediction of Z_w relative to the CIFER model causes a difference in phase at low frequencies.

$$\dot{w} = Z_w w + M_{\delta_{\text{col}}} \delta_{\text{col}} \tag{36}$$

Table 3: Hover heave stability and control derivatives of the UP Hexacopter

Derivative (Unit)	CIFER	RMAC
Z_w (1/s)	-0.338	-0.7313
$Z_{\delta_{\text{col}}}$ (m/s^2)	-39.4	-47.1

The longitudinal dynamics couple the surge velocity with the pitch attitude and pitch rate, and takes the form of Eq. 37, and the values of the relevant stability and control derivatives are tabulated in Table 4. RMAC correctly predicts the magnitude of the derivative M_u, but overpredicts the magnitude of $M_{\delta_{\text{lon}}}$ and the pitch damping, relative to the identified model. The transfer function from longitudinal stick input to pitch rate is represented in the Bode plot of Fig. 16. RMAC predictions capture the changes in magnitude and phase with the frequency of input well, especially above 4 rad/s.

$$\begin{Bmatrix} \dot{u} \\ \dot{q} \\ \dot{\theta} \end{Bmatrix} = \begin{bmatrix} X_u & 0 & -g \\ M_u & M_q & 0 \\ 0 & 0 & 1 \end{bmatrix} \begin{Bmatrix} u \\ q \\ \theta \end{Bmatrix} + \begin{bmatrix} 0 \\ M_{\delta_{\text{lon}}} \\ 0 \end{bmatrix} \delta_{\text{lon}} \tag{37}$$

The lateral dynamics (which take the form of Eq. 38) predicted by RMAC are identical to the longitudinal dynamics,

Table 4: Hover longitudinal stability and control derivatives of the UP Hexacopter

Derivative (Unit)	CIFER	RMAC
X_u (1/s)	-0.22	-0.052
M_u (rad/m s)	4.0	2.47
M_q (1/s)	0	-1.95
$M_{\delta_{\text{lon}}}$ (rad/s^2)	165	250

due to the symmetry of the aircraft (the difference between $M_{\delta_{\text{lon}}}$ and $L_{\delta_{\text{lat}}}$ is due to the mixer). The identified lateral dynamics are also similar. The stability and control derivatives are tabulated in Table 5, and a Bode plot of the transfer function is given in Fig. 17. As in pitch, RMAC predicts the lateral dynamics of the hexacopter well.

$$\begin{Bmatrix} \dot{v} \\ \dot{p} \\ \dot{\phi} \end{Bmatrix} = \begin{bmatrix} Y_v & 0 & g \\ L_v & L_p & 0 \\ 0 & 0 & 1 \end{bmatrix} \begin{Bmatrix} v \\ p \\ \phi \end{Bmatrix} + \begin{bmatrix} 0 \\ L_{\delta_{\text{lat}}} \\ 0 \end{bmatrix} \delta_{\text{lat}} \tag{38}$$

Table 5: Hover lateral stability and control derivatives of the UP Hexacopter

Derivative (Unit)	CIFER	RMAC
Y_v (1/s)	-0.22	-0.052
L_v (rad/m s)	-4.0	-2.47
L_p (1/s)	0	-1.95
$L_{\delta_{\text{lat}}}$ (rad/s^2)	145	217

Finally, the directional dynamics are described by the first-order Eq. 39, with stability and control derivatives tabulated in Table 6. Qualitatively, the fit is excellent for frequencies above 1 rad/s. The model-following cost (Ref. 35) for each of the four transfer functions is tabulated in Table 7. Generally, model-following costs below 100 are considered acceptable, and costs under 50 are nearly indistinguishable from the true aircraft response. Aside from the response from longitudinal stick to pitch rate, all of the hover transfer functions have costs below 100, suggesting that RMAC produces adequate models for control design about hover, when motor lag and input delay are included.

$$\dot{r} = N_r r + N_{\delta_{\text{ped}}} \delta_{\text{ped}} \tag{39}$$

Table 6: Hover directional stability and control derivatives of the UP Hexacopter

Derivative (Unit)	CIFER	RMAC
N_r (1/s)	0	-0.14
$N_{\delta_{\text{ped}}}$ (rad/s^2)	-22.9	12.9

Table 7: Model-Following Cost in Hover

Transfer Function	Cost	Frequency Range (rad/s)
Heave	68.0	0.6-25
Longitudinal	136.2	5-50
Lateral	90.8	5-50
Directional	45.6	1.5-20

Forward Flight Dynamics In forward flight, the symmetry of the aircraft is lost, and the longitudinal and lateral dynamics are no longer identical. Additionally, the longitudinal dynamics couple to the heave dynamics, and the lateral dynamics couple to the directional dynamics.

The coupled heave-longitudinal dynamics can be described by Eq. 40, where θ_5 represents the pitch attitude (positive nose-up) in trimmed flight. The predicted and identified stability derivatives are tabulated in Table 8. The on-axis stability derivatives (i.e. Z_w for heave and M_u for longitudinal) and control derivatives ($Z_{\delta_{\text{col}}}$ for heave and $M_{\delta_{\text{lon}}}$ for longitudinal) predictions generally agree on sign and magnitude, though off-axis (i.e. Z_u, M_w, and $M_{\delta_{\text{col}}}$) often do not. One possible reason is that while acquiring flight data, one axis is perturbed while leaving the feedback controllers on the other axes completely unchanged. Despite these differences, RMAC predictions of input-output transfer functions correlate well with the flight data at high frequency, as shown for heave in Fig. 19 and for pitch in Fig 20.

$$\begin{Bmatrix} \dot{u} \\ \dot{w} \\ \dot{q} \\ \dot{\theta} \end{Bmatrix} = \begin{bmatrix} X_u & X_w & 5\sin\theta_5 & -g\cos\theta_5 \\ Z_u & Z_w & 5\cos\theta_5 & g\sin\theta_5 \\ M_u & M_w & M_q & 0 \\ 0 & 0 & 1 & 0 \end{bmatrix} \begin{Bmatrix} u \\ w \\ q \\ \theta \end{Bmatrix} + \begin{bmatrix} 0 & 0 \\ Z_{\delta_{\text{col}}} & 0 \\ M_{\delta_{\text{col}}} & M_{\delta_{\text{lon}}} \end{bmatrix} \begin{Bmatrix} \delta_{\text{col}} \\ \delta_{\text{lon}} \end{Bmatrix} \tag{40}$$

Table 8: Forward Flight longitudinal stability and control derivatives of the UP Hexacopter

Derivative (Unit)	CIFER	RMAC
X_u (1/s)	-0.30	-0.35
X_w (1/s)	0	0.01
Z_u (1/s)	0	-0.44
Z_w (1/s)	-0.54	-1.22
M_u (rad/ m s)	2.05	1.24
M_w (rad/ m s)	-0.31	1.65
M_q (1/s)	-0.36	-2.63
$Z_{\delta_{\text{col}}}$ (m/s^2)	-39.5	-43.58
$M_{\delta_{\text{col}}}$ (rad/s^2)	-5.51	8.84
$M_{\delta_{\text{lon}}}$ (rad/s^2)	156	201

The coupled lateral and directional dynamics can be described by Eq. 41, with stability and control derivatives given by Table 9. The transfer functions are plotted in Fig. 21 for roll and lateral stick, and Fig. 22 for yaw rate and pedal input. Model following costs at 5 m/s forward flight are listed in Table 10. Heave and directional dynamics are predicted with a model-following cost below 100, while longitudinal and lateral dynamics are predicted with costs around 130. Though improvement in the latter is desirable, RMAC produces reasonable estimates of the dynamics, particularly at high frequency without need for the physical hardware necessary for system identification.

$$\begin{Bmatrix} \dot{v} \\ \dot{p} \\ \dot{r} \\ \dot{\phi} \end{Bmatrix} = \begin{bmatrix} Y_v & -5\sin\theta_5 & -5\cos\theta_5 & g\cos\theta_5 \\ L_v & L_p & L_r & 0 \\ 0 & 0 & N_r & 0 \\ 0 & 0 & 1 & -\sin\theta_5 \end{bmatrix} \begin{Bmatrix} v \\ p \\ r \\ \phi \end{Bmatrix} + \begin{bmatrix} 0 & 0 \\ L_{\delta_{\text{lat}}} & L_{\delta_{\text{ped}}} \\ 0 & N_{\delta_{\text{ped}}} \end{bmatrix} \begin{Bmatrix} \delta_{\text{lat}} \\ \delta_{\text{ped}} \end{Bmatrix} \quad (41)$$

Table 9: Forward flight lateral stability and control derivatives of the UP Hexacopter

Derivative (Unit)	CIFER	RMAC
Y_v (1/s)	-0.30	-0.20
L_v (rad/ m s)	-3.18	-1.81
L_p (1/s)	-0.90	-2.62
L_r (1/s)	0	1.02
N_r (1/s)	-0.51	-0.14
$L_{\delta_{\text{lat}}}$ (rad/s^2)	141	174
$L_{\delta_{\text{ped}}}$ (rad/s^2)	0	-6.55
$N_{\delta_{\text{ped}}}$ (rad/s^2)	-22.3	10.11

Table 10: Model-following cost RMAC predictions of for the UP hexacopter at 5 m/s forward speed

Transfer Function	Cost	Frequency Range (rad/s)
Heave	82.1	5-22
Pitch	139	5-50
Lateral	123	5-34
Directional	56.5	5-20

CONCLUSIONS

A comprehensive analysis code for multicopters has been developed and presented. It is capable of predicting isolated rotor forces and moments, as well as determining trim on a user-defined aircraft with a variety of different aerodynamic models. RMAC analyses of the SUI Endurance rotor has been validated against experimental data and high-fidelity CFD analyses, finding that RMAC results are within 5% of CAMRAD predictions in hover, and captures loading trends in forward flight.

RMAC can also produce linearized models that can be used for control design. On the University of Portland Hexacopter, RMAC-generated models have been compared to linear models identified from flight data by CIFER. In hover, the RMAC models agree very well with flight data along all four axes, and captures the real system well enough to develop controllers. In forward flight, RMAC faithfully captures the transfer functions from the control inputs to the heave acceleration and rotational rates, except for heave at low frequency, where there is a significant deviation, which may be due to an inaccurate estimation of the off-axis stability and control derivatives from the flight data. Overall, the RMAC predictions are sufficient for linear control design, with model-following costs below 100 in hover for heave, roll, and yaw in hover, and costs below 100 for heave and yaw in forward flight.

Author contact: Robert Niemiec niemir2@rpi.edu; Farhan Gandhi, fgandhi@rpi.edu

ACKNOWLEDGMENTS

This work is carried out at the Rensselaer Polytechnic Institute under the Army/Navy/NASA Vertical Lift Research Center of Excellence (VLRCOE) Program, grant number W911W61120012, with Dr. Mahendra Bhagwat and Dr. William Lewis as Technical Monitors.

REFERENCES

[1]"EHang 216 - Electric VTOL News," URL: http://evtol.news/aircraft/ehang-216/, 2018, [retrieved 3 August 2018].

[2]"Cora," URL: https://cora.aero, [retrieved 3 August 2018].

[3]"Volocopter - Home," URL: https://www.volocopter.com/en/, [retrieved 25 July 2018].

[4]"Joby S4–Electric VTOL News," URL: http://evtol.news/aircraft/joby-aviation/, 2018, [retrieved 25 July 2018].

[5]"Amazon Prime Air," URL: https://www.amazon.com/b?node=8037720011, [retrieved 25 July 2018].

[6]"Project Wing - Project Wing," URL: https://x.company/wing/, [retrieved 25 July 2018].

[7]"Boeing Cargo Air Vehicle - Electric VTOL News," URL: http://evtol.news/aircraft/boeing-cav/, 2018, [retrieved 3 August 2018].

[8]Parsons, D., "Meet Bell Nexus, The Six-Ducted-Fan Air Taxi of the Future," URL: https://www.rotorandwing.com/2019/01/07/meet-bell-nexus-six-ducted-fan-air-taxi-future/, Jan. 2019.

[9]"Fast-Forwarding to a Future of On-Demand Urban Air Transportation [online]," URL: https://www.uber.com/elevate.pdf, 2016, [retrieved 25 July 2018].

[10]NASA, "ARMD Urban Air Mobility Grand Challenge UAM Grand Challenge Scenarios," Oct. 2018.

[11]Bouabdallah, S., Murrieri, P., and Siegwart, R., "Design and Control of an Indoor Micro Quadrotor," *Proceedings of the 2004 IEEE International Conference on Robotics and Automation*, Institute of Electrical and Electronics Engineers, 2004, pp. 4393–4398.

[12]Mueller, M. and D'Andrea, R., "Stability and Control of a Quadrocopter Despite the Complete Loss of One, Two, or Three Propellers," *IEEE International Conference on Robotics and Automation*, International Electrical and Electronics Engineers, 2014 2014, pp. 45–52.

[13]Deters, R. and Selig, M., "Static Testing of Micro Propellers," *26th AIAA Applied Aerodynamics Conference*, No. AIAA 2008-6246, 2018.

[14]Yoon, S., Diaz, P., Boyd, D. D., Chan, W., and Theodore, C., "Computational Aerodynamic Modeling of Small Quadcopter Vehicles," *73rd Annual Forum of the American Helicopter Society International*, No. 73-2017-0015, American Helicopter Society International, 2017.

[15]Misiorowski, M., Gandhi, F., and Oberai, A., "A Computational Study on Rotor Interactional Effects for a Quadcopter in Edgewise Flight," *74th Annual Forum of the American Helicopter Society*, No. 74-2018-1266, American Helicopter Society International, 2018.

[16]Leishman, J. G., *Principles of Helicopter Aerodynamics*, chap. 2, 10, Cambridge University Press, New York, 2nd ed., 2006.

[17]"RCAS Theory Manual, Version 2.0," Tech. Rep. USAAMCOM/ADFF TR 02-A-005, United States (US) Army Aviation and Missile COmmand/AeroFlightDynamics Directorate (USAAMCOM/AFDD), June 2002.

[18]Johnson, W., *CAMRAD II, Comprehensive Analytical Model of Rotorcraft Aerodynamics and Dynamics*, Johnson Aeronautics, 1992.

[19]Bir, G., Chopra, I., Ganguli, R., Smith, E., Villaichamy, S., Wang, J., Kim, K., Chan, W. Y., Nixon, M., Kimata, N., Smith, J., Torok, M., and Nguyen, K., "University of Maryland Advanced Rotorcraft Code," Tech. Rep. UM-AERO 94-18, University of Maryland, July 2016.

[20]Niemiec, R. and Gandhi, F., "Effect of Rotor Cant on Trim and Autonomous Flight Dynamics of a Quadcopter," *74th Annual Forum of the American Helicopter Society*, No. 74-2018-0178, American Helicopter Society International, 2018.

[21]Johnson, W., *Helicopter Aeromechanics*, chap. 5, Cambridge University Press, New York, 2013.

[22]Niemiec, R. and Gandhi, F., "Effect on Inflow Model on Simulated Aeromechanics of a Quadrotor Helicopter," *72nd Annual Forum of the American Helicopter Society International*, No. 72-2016-370, American Helicopter Society International, 2016.

[23]Peters, D., Boyd, D., and He, C. J., "Finite-State Induced-Flow Model for Rotors in Hover and Forward Flight," *Journal of the American Helicopter Society*, Vol. 34, No. 4, 1989, pp. 5–17.

[24]Díaz, P., Yoon, S., and Theodore, C., "High-Fidelity Computational Aerodynamics of the Elytron 4S UAV," *AHS Technical Conference on Aeromechanics Design for Transformative Vertical Flight*, No. sm_aeromech_2018_02, American Helicopter Socety International, 2018.

[25]Bhagwat, M., *Transient Dynamics of Helicopter Rotor Wakes Using a Time-Accurate Free-Vortex Method*, Ph.D. thesis, University of Maryland, College Park, 2001.

[26]Bagai, A., *Contributions to the Mathematical Modeling of Rotor Flow-Fields Using a Pseudo-Implicit Free-Wake Analysis*, Ph.D. thesis, University of Maryland, College Park, 1995.

[27]Hodges, D. and Dowell, E., "Nonlinear Equations of Motion for the Elastic Bneding and Torsion of Twisted Nonuniform Rotor Blades," Technical Note TN D-7818, National Aeronautics and Space Administration, December 1974.

[28]Hohenemser, K. H. and Yin, S.-K., "Some Applications of the Method of Multiblade Coordinatse," *Journal of the American Helicopter Society*, Vol. 17, No. 3, July 1972, pp. 3–12.

[29]Niemiec, R. and Gandhi, F., "Multi-rotor Coordinate Transforms for Orthogonal Primary and Redundant Control Modes for Regular Hexacopters and Octocopters," *42nd European Rotorcraft Forum*, No. 111bis, La Société Savante de l'Aéronautique et de l'Espace, 2016.

[30]Corson, D., Griffith, D. T., Ashwill, T., and Shakib, F., "Investigating Aeroelastic Performance of Multi-MegaWatt Wind Turbine Rotors Using CFD," No. AIAA Paper 2012-1827, 2012.

[31]"Products — STRAIGHT UP IMAGING," URL: http://www.straightupimaging.com/products/, [retrieved 25 July 2018].

[32]Russell, C., Willink, G., Theodore, C., Jung, J., and Glasner, B., "Wind tunnel and Hover Performance Test Results for Multicopter UAS Vehicles," Tech. Rep. NASA/TM-2018-219758, National Aeronautics and Space Administration, 2018.

[33]Tischler, M. and Remple, R., *Aircraft and Rotorcraft System Identification.*, AIAA, 2nd ed., 2012.

[34]Ivler, C., Niemiec, R., and Gandhi, F., "REPLACE WITH ACTUAL TITLE," *75th Annual Forum of the Vertical Flight Society*, No. 75-2019-????, Vertical Flight Society, May 2019.

[35]Tischler, M., Berger, T., Ivler, C., Mansur, M., Cheung, K., and Soong, J., *Practical Methods for Aircraft and Rotorcraft Flight Control Design: An Optimization-Based Approach*, chap. 5, AIAA Education Series.

FIGURES

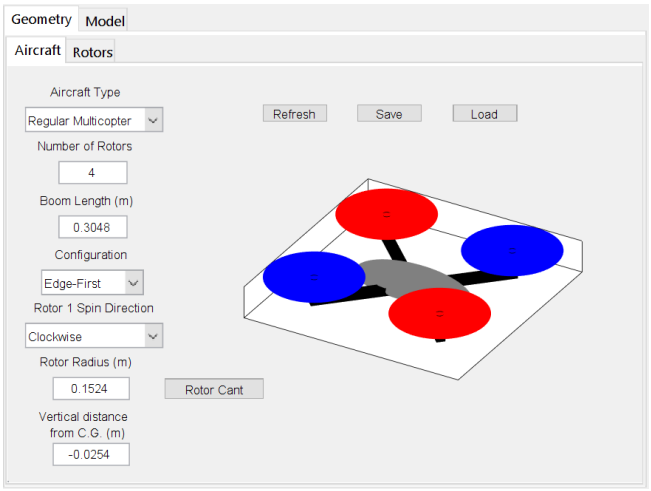

Fig. 1: Aircraft Geometry Definition GUI

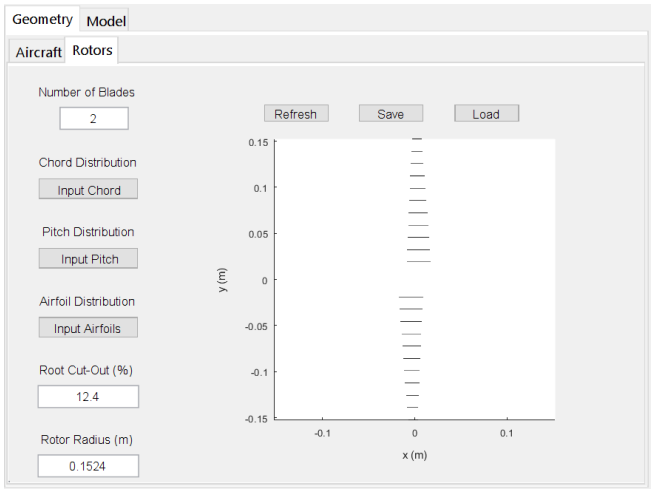

Fig. 2: Rotor Geometry Definition GUI

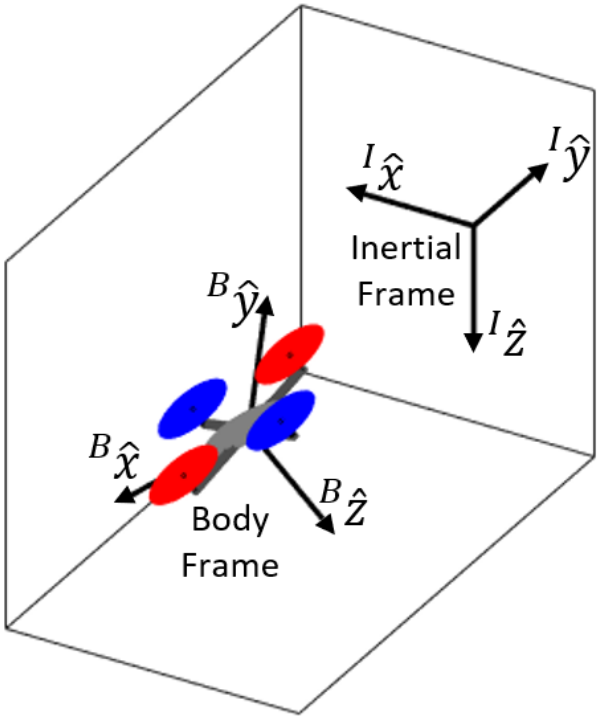

Fig. 3: Inertial and body reference frames

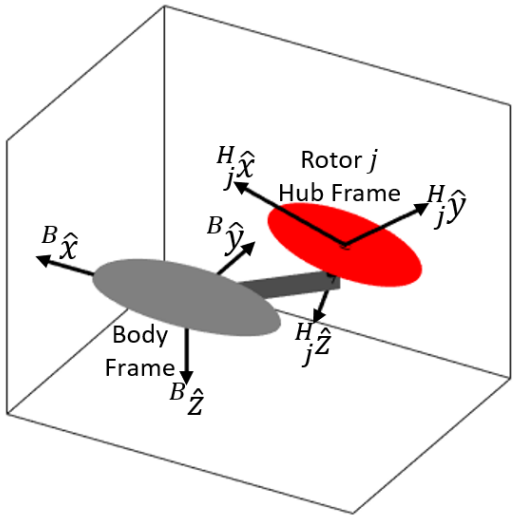

Fig. 4: Body and hub reference frames – only a single rotor is drawn for clarity

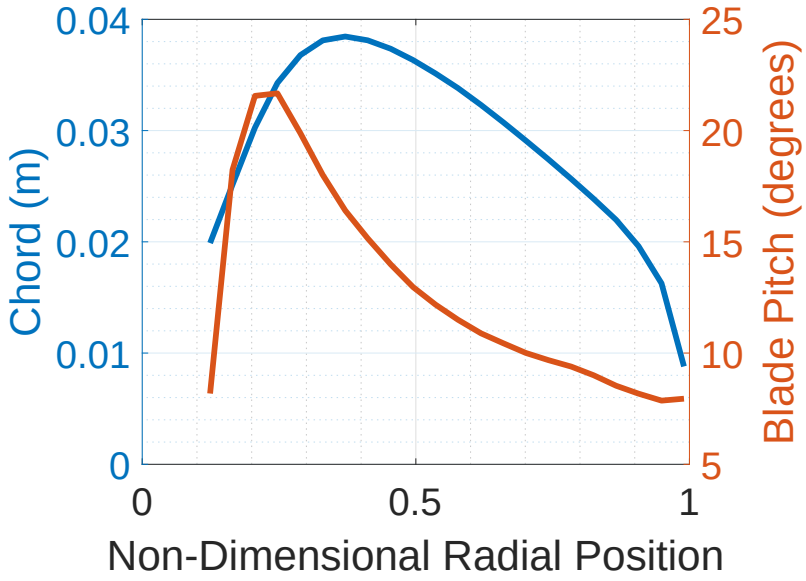

Fig. 5: SUI Endurance rotor geometry (Ref. 32)

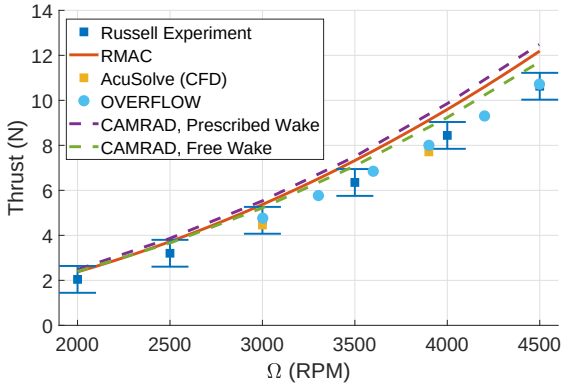

Fig. 6: RMAC predictions for SUI rotor hover thrust, compared to CAMRAD, AcuSolve, OVERFLOW, and experiment

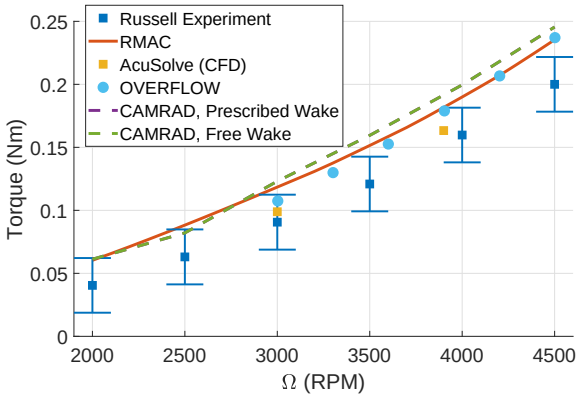

Fig. 7: RMAC predictions for SUI rotor hover torque, compared to CAMRAD, AcuSolve, OVERFLOW, and experiment

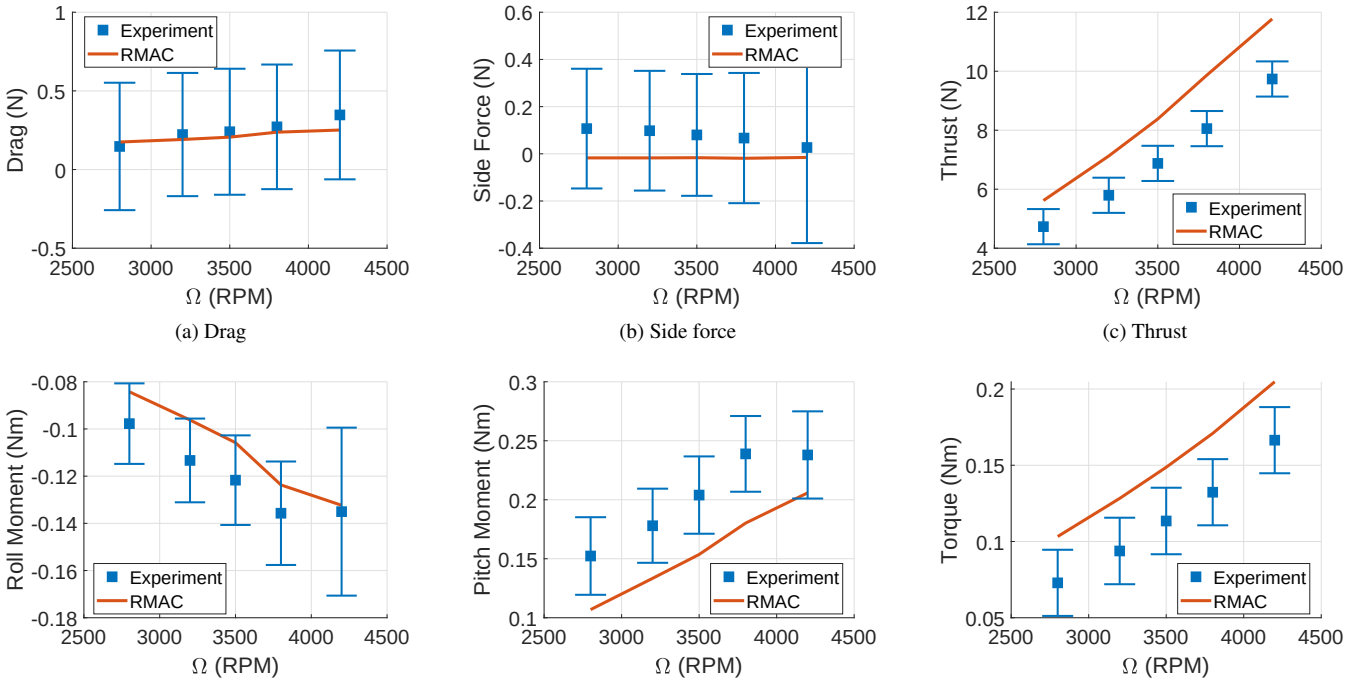

(a) Drag (b) Side force (c) Thrust

(d) Roll moment (e) Pitch moment (f) Torque

Fig. 8: RMAC predictions of SUI Rotor rotor forces and moments at 6.1 m/s wind speed versus experiment, nose-level

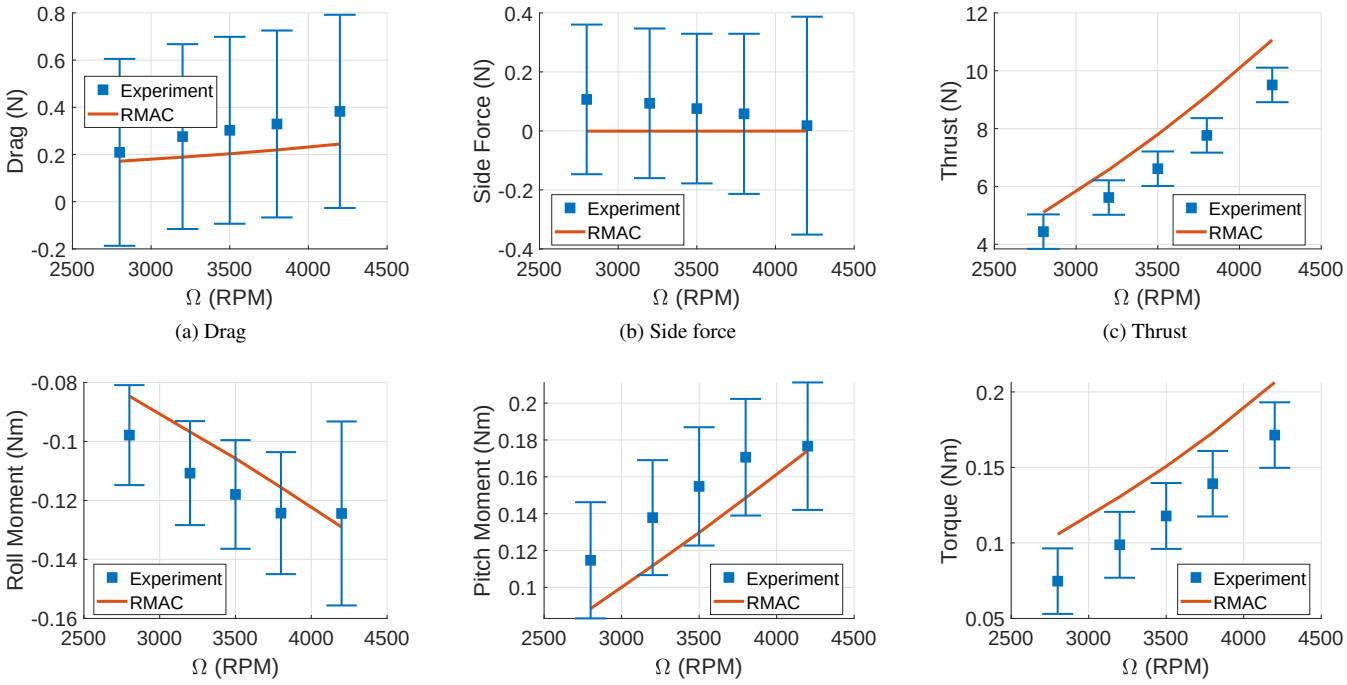

(a) Drag (b) Side force (c) Thrust

(d) Roll moment (e) Pitch moment (f) Torque

Fig. 9: RMAC predictions of SUI Rotor rotor forces and moments at 6.1 m/s wind speed versus experiment, 10 degrees nose-down

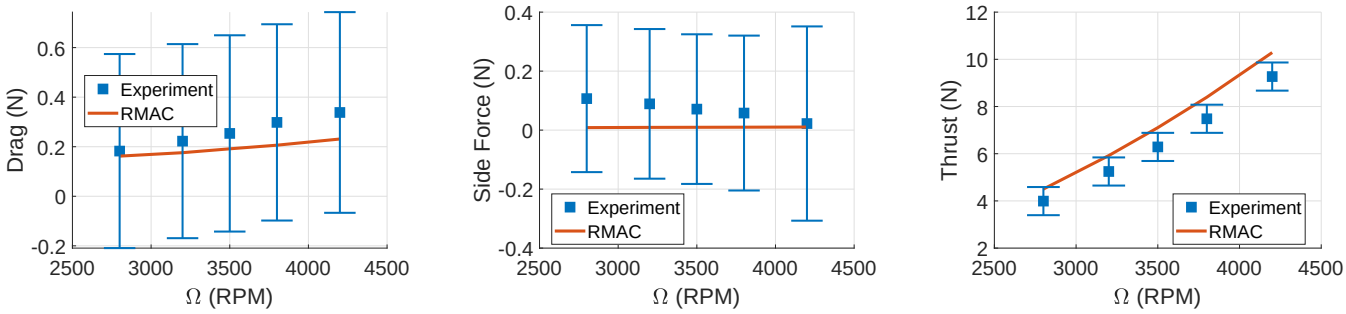

(a) Drag (b) Side force (c) Thrust

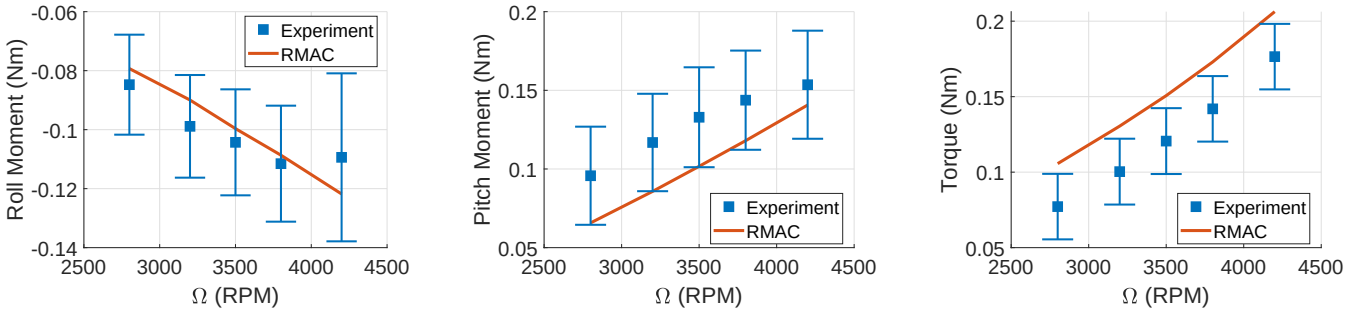

(d) Roll moment (e) Pitch moment (f) Torque

Fig. 10: RMAC predictions of SUI Rotor rotor forces and moments at 6.1 m/s wind speed versus experiment, 20 degrees nose-down

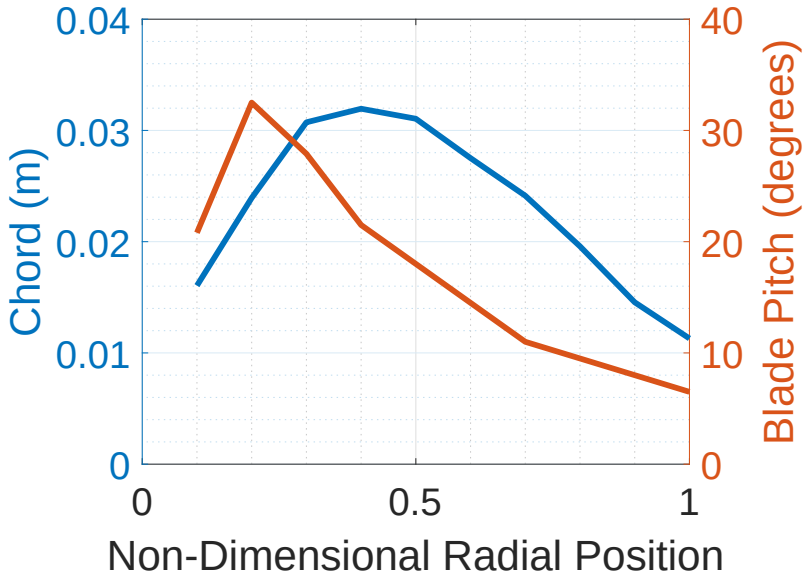

Fig. 11: AeroQuad Cyclone Rotor Geometry (Ref. 15)

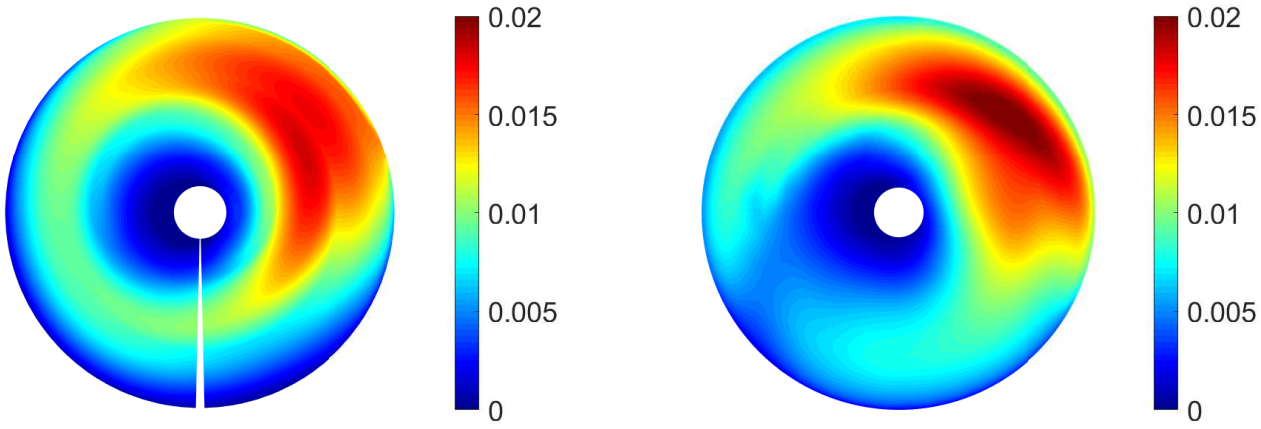

(a) RMAC (b) AcuSolve

Fig. 12: Thrust coefficient distribution predictions for AeroQuad Rotor at 4495 RPM, 10 m/s, and 5° nose-down attitude

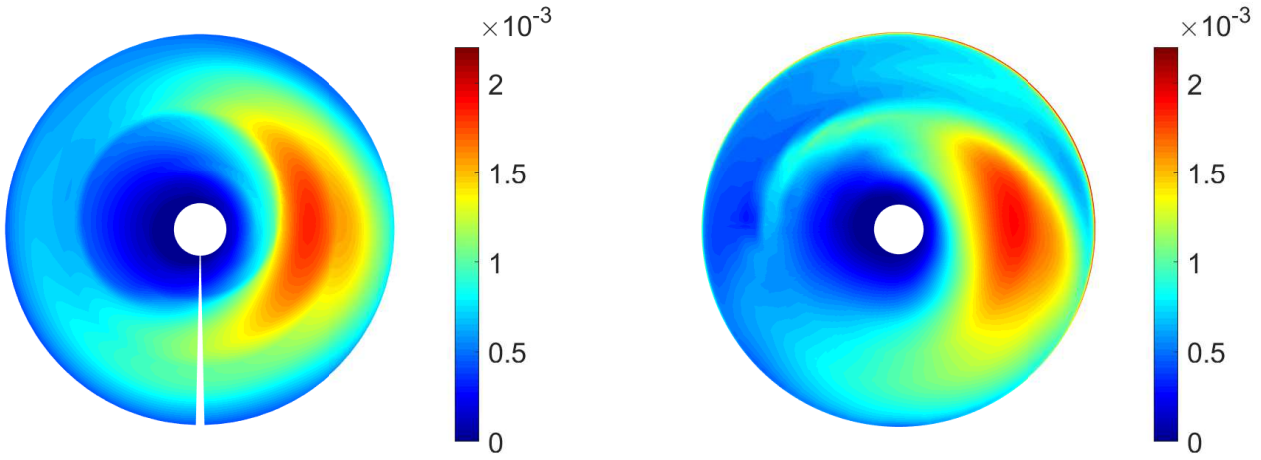

(a) RMAC (b) AcuSolve

Fig. 13: Torque coefficient distribution predictions for AeroQuad Rotor at 4495 RPM, 10 m/s, and 5° nose-down attitude

Fig. 14: University of Portland Hexacopter

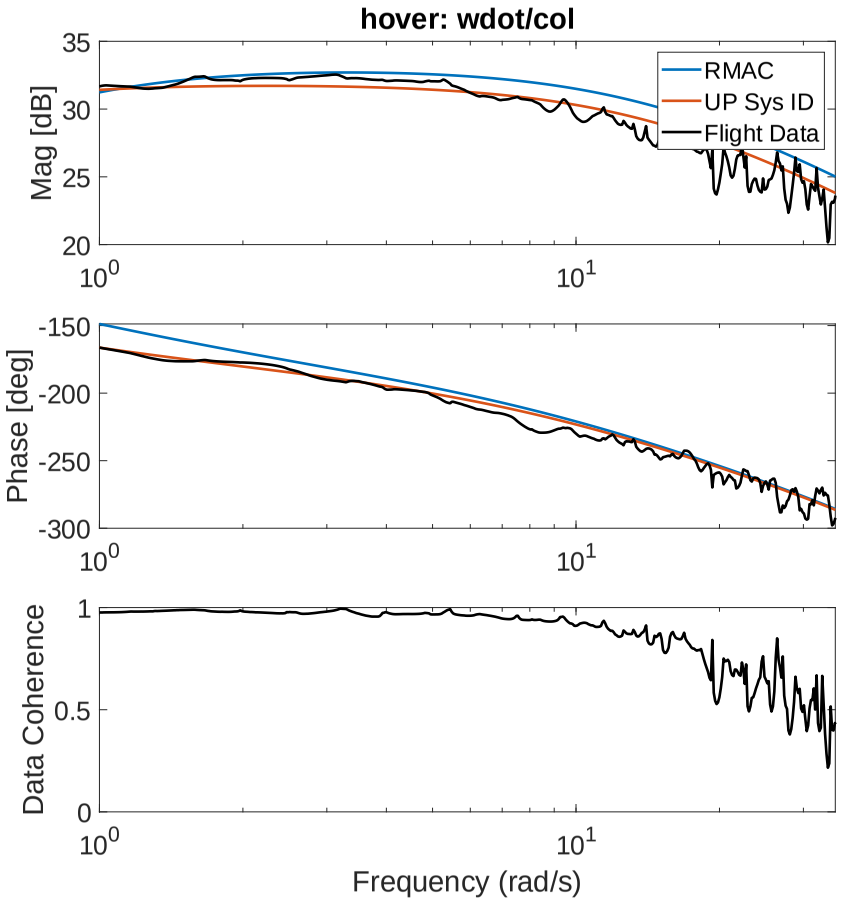

Fig. 15: Transfer function from collective input to heave for the UP Hexacopter in hover

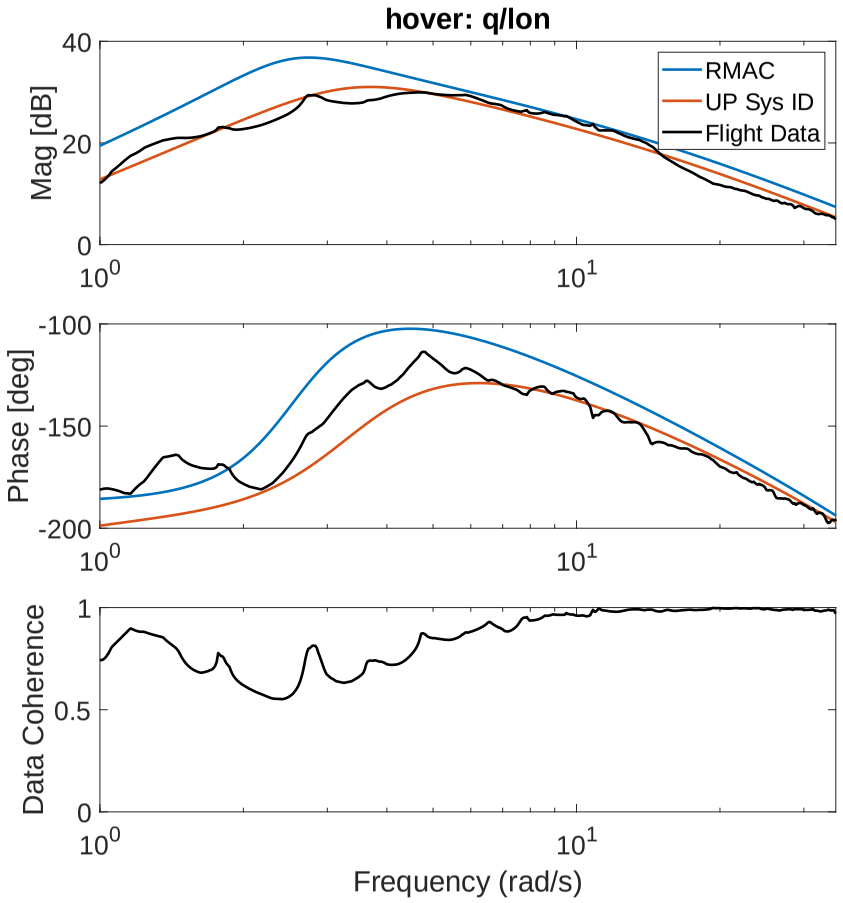

Fig. 16: Transfer function from longitudinal stick input to pitch rate for the UP Hexacopter in hover

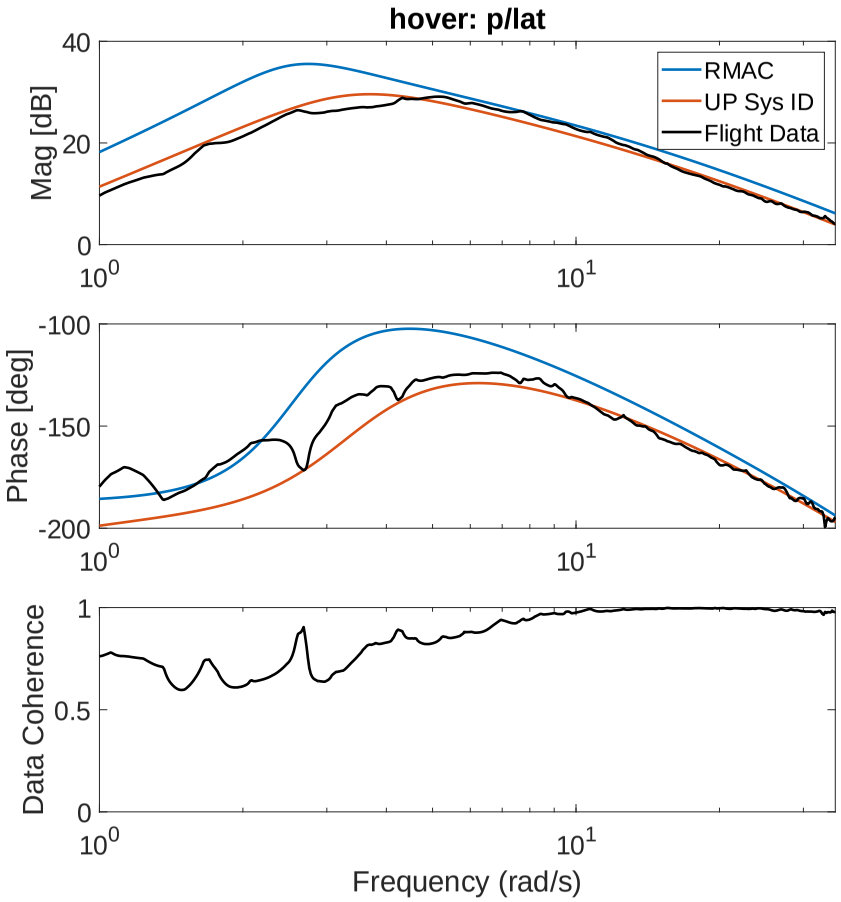

Fig. 17: Transfer function from lateral input to roll rate for the UP Hexacopter in hover

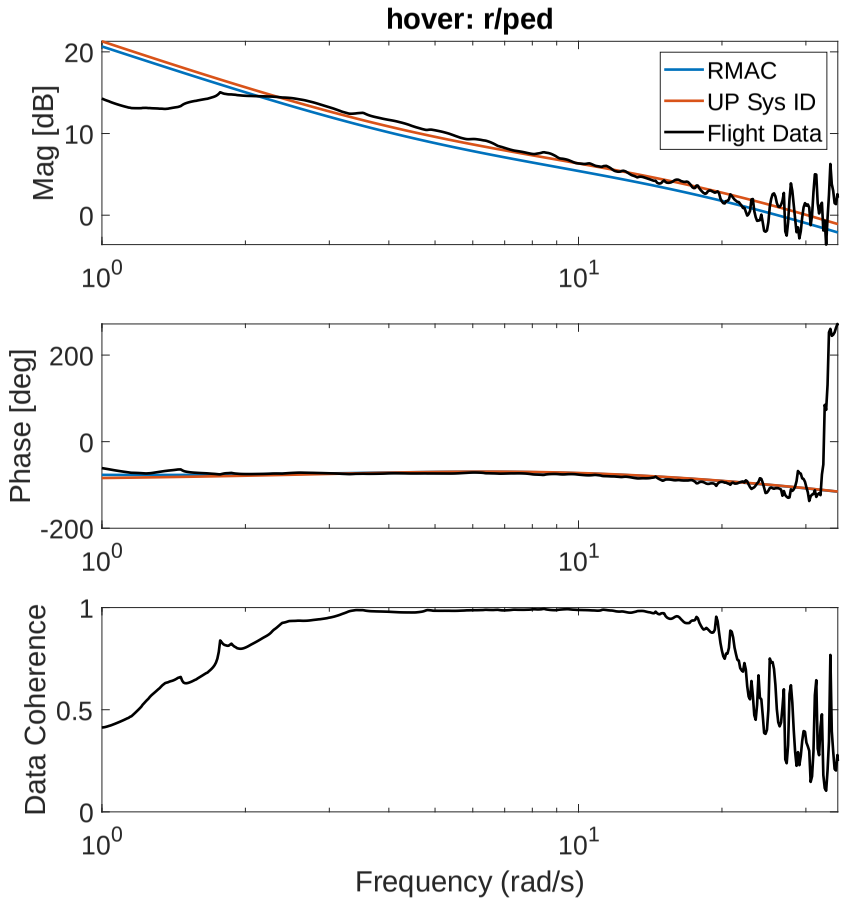

Fig. 18: Transfer function from pedal stick input to yaw rate for the UP Hexacopter in hover

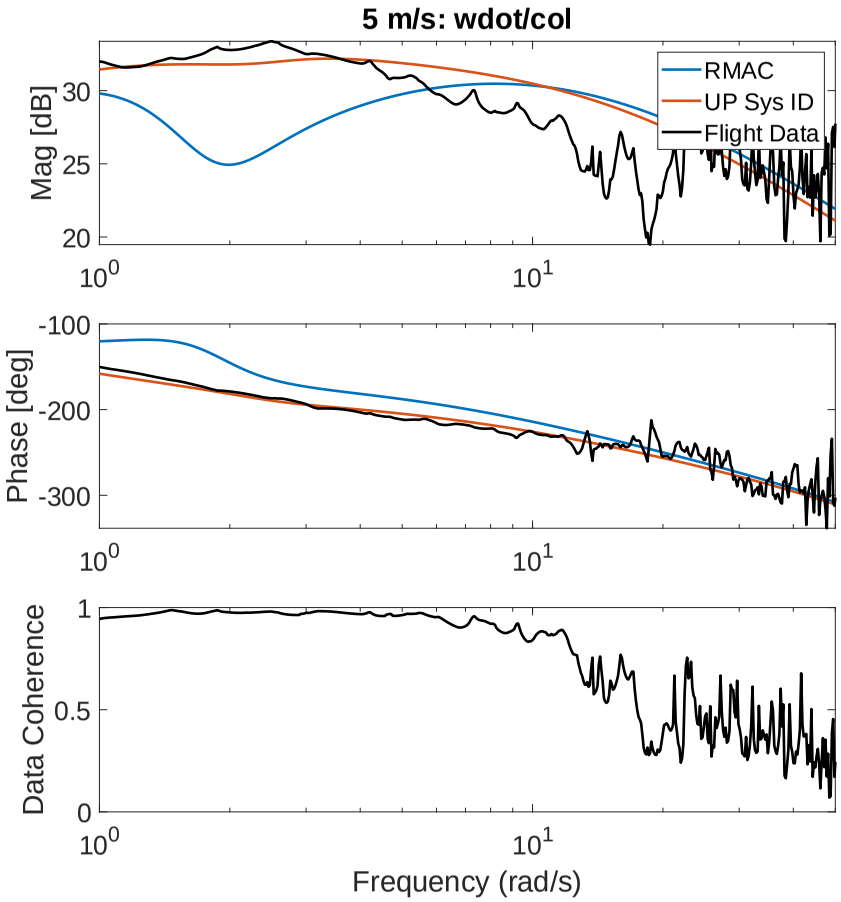

Fig. 19: Transfer function from collective input to heave acceleration for the UP Hexacopter at 5 m/s forward speed

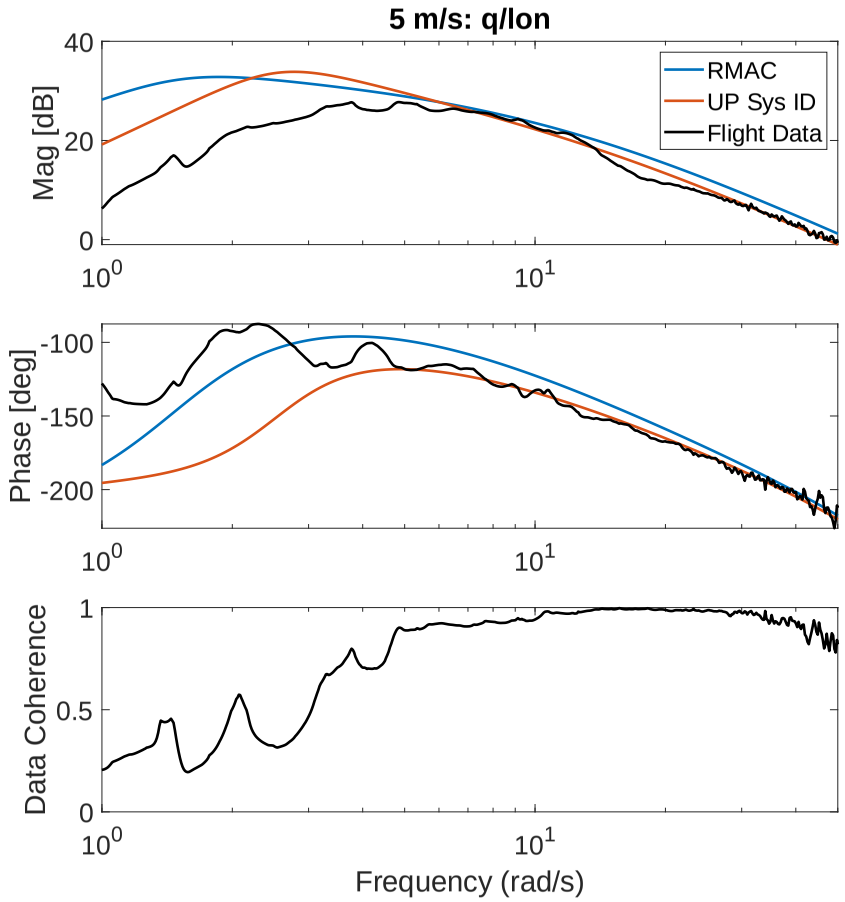

Fig. 20: Transfer function from longitudinal stick input to pitch rate for the UP Hexacopter at 5 m/s forward speed

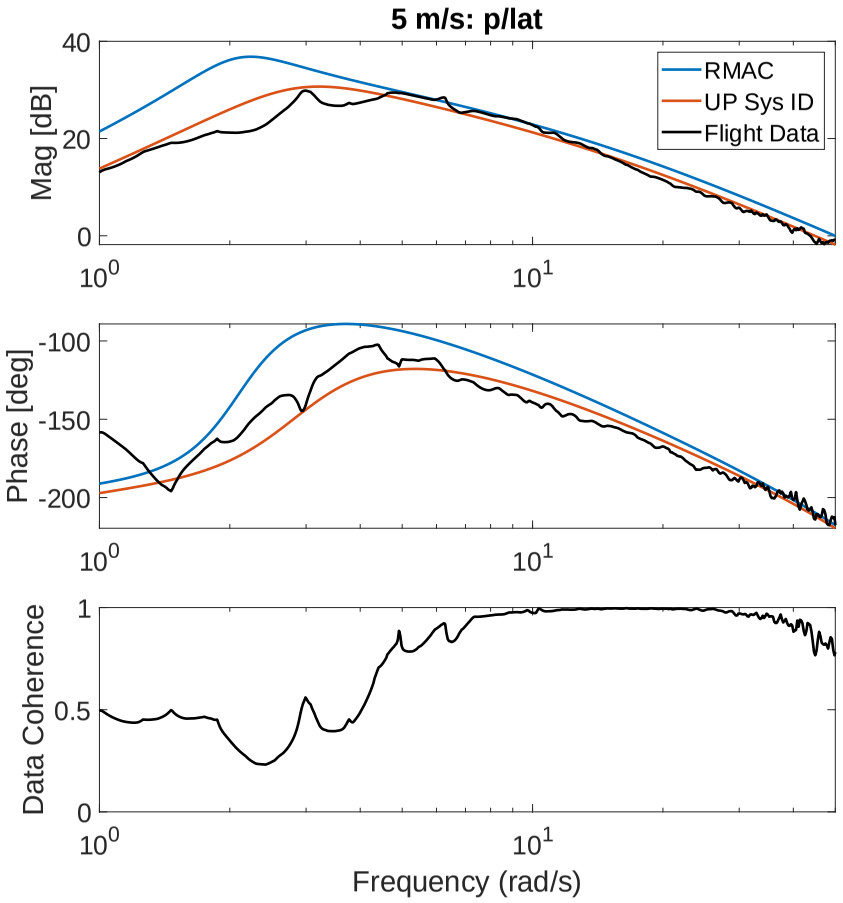

Fig. 21: Transfer function from lateral input to roll rate for the UP Hexacopter at 5 m/s forward speed

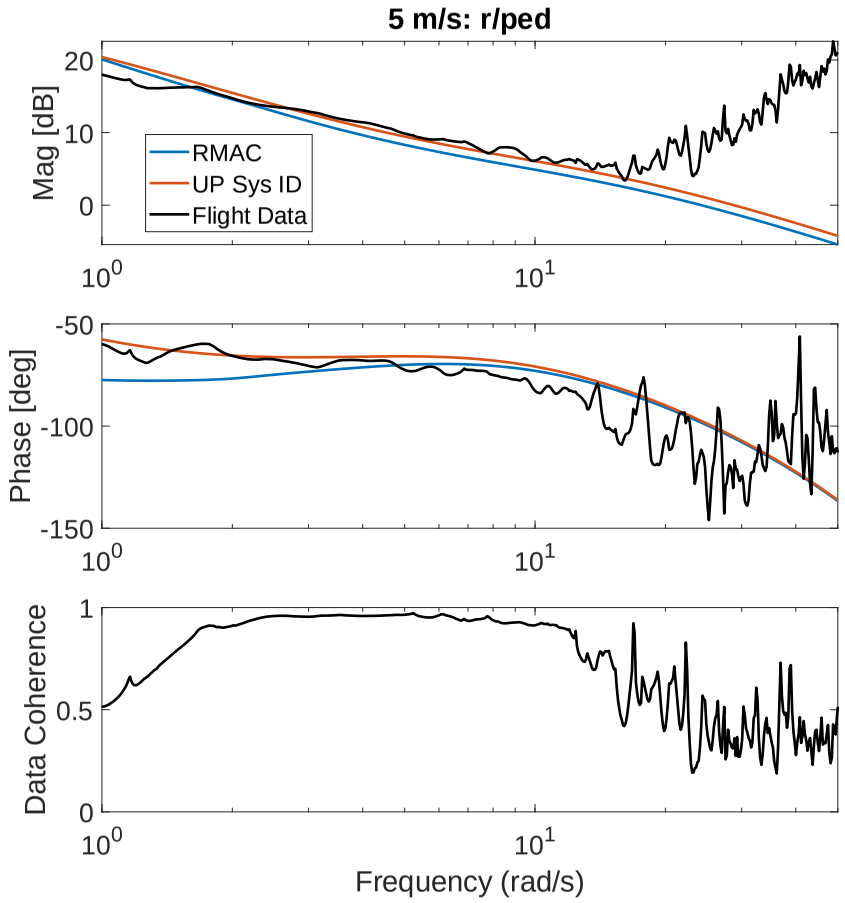

Fig. 22: Transfer function from pedal stick input to yaw rate for the UP Hexacopter at 5 m/s forward speed